JOURNAL OF GEOPHYSICAL RESEARCH VOL. 95, NO. C6, PAGES 9433–9445, JUNE 15, 1990

Enhancement of Fronts by Vertical Mixing

RICHARD K. DEWEY AND JAMES N. MOUM

College of Oceanography, Oregon State University, Corvallis

Microstructure observations near upwelled fronts indicate considerable variation in the structure of vertical mixing across the frontal region. Observations of cool filaments off northern California indicate that within the cool (dense) core of filaments the raised pycnocline inhibits the penetration to middepths of surface-generated mixing. The microstructure profiles are used to estimate the available wind energy for mixing as a function of pycnocline, or mixed layer depth. A greater portion of energy input at the surface is available for entrainment of dense fluid through the pycnocline and into the surface mixed layer where the pycnocline is shallow. Hence surface-forced mixing may cause a more rapid increase in mixed layer density within the cool filament than outside the filament, resulting in an enhanced horizontal density gradient in the mixed layer. Assuming the flow adjusts towards geostrophy, the enhanced horizontal density gradient at the front could result in an accelerated mixed layer in the direction of the preexisting geostrophic flow. Proportions relating the gain in potential energy to the wind energy vary with pycnocline depth and differ by as much as an order of magnitude from the findings of Denman and Miyake (1973) and Davis et al. (1981). Horizontal variability of pycnocline erosion may not be properly taken into account in some models and should more realistically be parameterized by including dependence on pycnocline depth.

1. INTRODUCTION

During spring and early summer (April–July) the northerly winds along the California coast induce coastal upwelling, bringing anomalously cool ($\delta T \sim 2°C$), saline ($\delta S \sim 2‰$) water to the surface, raising the pycnocline over the continental shelf. Satellite images have revealed large, cool features extending offshore beyond the shelf break, often hundreds of kilometers seaward of the upwelling region [e.g., *Bernstein et al.*, 1977; *Ikeda and Emery*, 1984; *Flament et al.*, 1985]. These anomalous features are believed to play a crucial role in the exchange of properties across the coastal transition zone, the region between the nearshore upwelling area and the offshore ocean [*Mooers and Robinson*, 1984]. These features were the focus of the Coastal Transition Zone (CTZ) experiment. The fronts observed were located west of Point Arena, California, seaward of the continental shelf.

During upwelling conditions, isopycnals dome over the shelf, and the southward flowing California Current develops along the continental shelf break [*Huyer* 1983; *Brink* 1983]. The strong current found along the sloping isopycnals is not confined to the shelf/slope region, and often features resembling meanders, squirts, jets, and eddies form on the western edge of the upwelled front [*Bernstein et al.*, 1977]. The cause of these features and the resulting influences that they impose on the local ocean are not understood. It is believed these features modify the exchange of water between the nearshore upwelling region and the offshore ocean. Direct transport, increased mesoscale eddy formation, turbulent diffusion, and intrusions near the frontal region are some of the possible mechanisms by which these variable structures enhance diffusion across the transition zone.

Observations of microscale processes indicate that the rate of surface-induced mixing may vary with proximity to the front and that the horizontal density gradients thus established may act to accelerate the mixed layer at the front. A series of detailed transects across a meander indicate that both water properties and dynamics vary with proximity to the front. We emphasize the distinction between "mixing layer depth" (the depth where the dissipation rate drops monotonically below some arbitrarily small value), and "mixed layer depth" (the depth at which density increases by some predetermined amount above the near surface value) and employ this important distinction in proposing a mechanism that enhances the cool surface temperatures and accelerates the surface layer by establishing horizontal density gradients in the surface layer through vertical mixing across the pycnocline.

The objective of this paper is to investigate the role that surface-induced mixing may play in maintaining and modifying the surface signature of observed structures in the transition zone. In the following pages we briefly review the measurements, describe the large-scale structure, and investigate the dynamics resulting from enhanced pycnocline erosion within a meander observed in June 1987. Variations in mixed layer depth across the frontal region are considerable (~2 to 60 m). The flux of turbulent kinetic energy into the surface layer from wind forcing is dissipated by viscous effects and, in the presence of stratification, converted into potential energy by turbulent buoyancy fluxes. Variations in these energy sinks are investigated across the frontal region, and the observations are compared against various parameters used in surface layer models. The role of turbulent mixing in maintaining the surface signature of the fronts is investigated, and a possible mechanism is proposed to accelerate the surface layer in the frontal region.

2. INSTRUMENTATION AND DATA PROCESSING

The data discussed here were collected in June 1987 and represent a portion of the microstructure surveys associated with the CTZ program. Profiles to 200 m of temperature, salinity, density, and turbulent dissipation rate (ε) were determined from the freely falling microstructure profiler, rapid-sampling vertical profiler (RSVP) [*Caldwell et al.*, 1985]. At ship speeds of 2–3 knots (1–1.5 m s^{-1}), for the transects discussed here, RSVP profiles were made at hori-

Paper number 90JC00271.
0148-0227/90/90JC-00271$05.00

zontal separations of 800–1200 m. An acoustic Doppler current profiler (ADCP) mounted on the hull of R/V *Wecoma* was used to measure current velocities (U and V) from 15 m to 200 m. Additional measurements included continuous sea surface (~3 m) temperature and conductivity from the ship's sea chest. Meteorological measurements included wind speed and direction, incoming solar and infrared radiation, air temperature, and humidity, recorded every 2 min and averaged every hour. Bulk formula estimates were made of latent and sensible heat fluxes, long-wave backscatter radiation, and surface buoyancy flux, J_b^o.

The hull-mounted ADCP was set to transmit 16-ms pulses and to receive range-gated bins of 6.2 ms, resulting in vertical depth bins of 4 m [*Chereskin et al.*, 1986]. The shallowest bin uncontaminated by source noise was centered at 15.1 m depth, with independent observations at three-bin (12 m) intervals. The Doppler data were averaged into 15-min profiles. To obtain absolute velocities, navigation data were used to estimate absolute ship velocity. Three independent navigation systems collected data during the cruise (two Loran-C systems as well as intermittent coverage by Global Positioning System satellites). The three were combined to obtain the best estimates of true positions. These estimates were smoothed with a 15-min filter and ship velocity estimates obtained by first-differencing. Absolute current velocities were then calculated by adding the ship velocity to the relative current profiles. We estimate errors in the final current velocities to be less than 5 cm s^{-1}.

3. Large-Scale Structure

The large-scale (mesoscale) structure of the features being investigated is most easily visualized by satellite imagery. Unfortunately, due to cloud cover, satellite images are unavailable for the period covering the three transects presented here. The nearest clear image was collected 2 days prior to our arrival at 39.7°N, 125°W (Figure 1). Starting June 3, 1987, a sequence of three transects were made along 125°W, from 39.7°N to 37.9°N, each crossing the cool feature extending west of Point Arena (Figure 1). Transects 1 and 3 were run from north to south (right to left for contour plots), whereas transect 2 was run from south to north (left to right). Each transect took approximately 26 hours to complete.

Light (~4 m s^{-1}) southerly winds during the first two transects were followed by stronger (~13 m s^{-1}) northerly winds during the third transect (Figure 2*a*). The time of day during which measurements were made is roughly indicated by the surface buoyancy flux J_b^o (Figure 2*b*), which was dominated by incoming solar radiation (negative contribution) and latent heating (positive contribution). It will be assumed in the following discussion that the surface buoyancy flux varies on synoptic scales only and will not contribute to fine-scale heating or cooling.

The frontal feature of interest can be identified in the advanced very high resolution radar (AVHRR) image (Figure 1) west of Point Arena. Figures 3*a*, 3*b*, 3*c*, 3*d*, and 3*e* are transect contours of σ_t, temperature, salinity, zonal velocity, and log ε, respectively, collected along 125°W between 37.9° and 39.7°N. The meanderlike structure is identifiable in the contour plots by a cool, saline (dense) core. Shallowing isopycnals toward the center of the core result in pycnocline depths that vary by as much as 60 m across the feature.

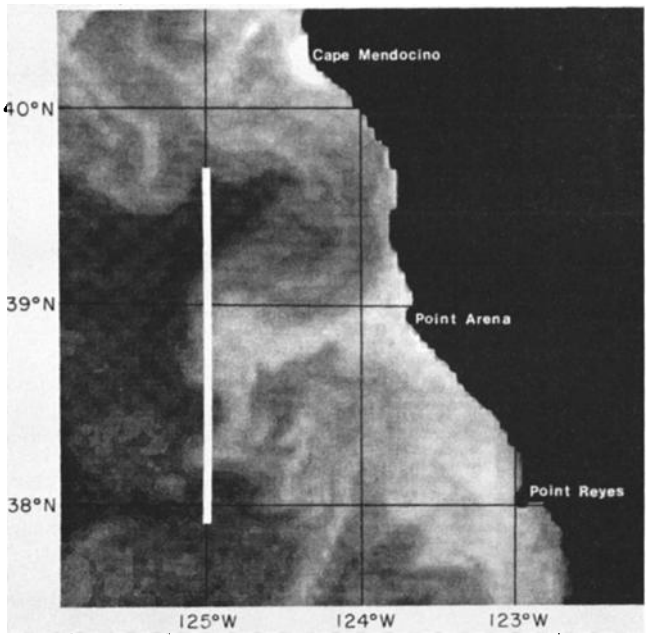

Fig. 1. AVHRR image of the Coastal Transition Zone area west of California, showing Cape Mendocino to the north, Point Arena and Point Reyes to the south. The image was obtained at 1400 June 1, 1987, local time. Three in situ transects made along 125°W from 37.9 to 39.7°N on June 3, 4, and 5, 1987.

Upward sloping isopycnals to the north of the meander represent the southern portion of an onshore flow southwest of Cape Mendocino (Figure 1).

Toward the north end of transect 2, and during transect 3, winds increased (from <5 to 13 m s^{-1}), and significant modification of the near-surface region is attributable to wind-induced mixing. The near-surface isopycnals are

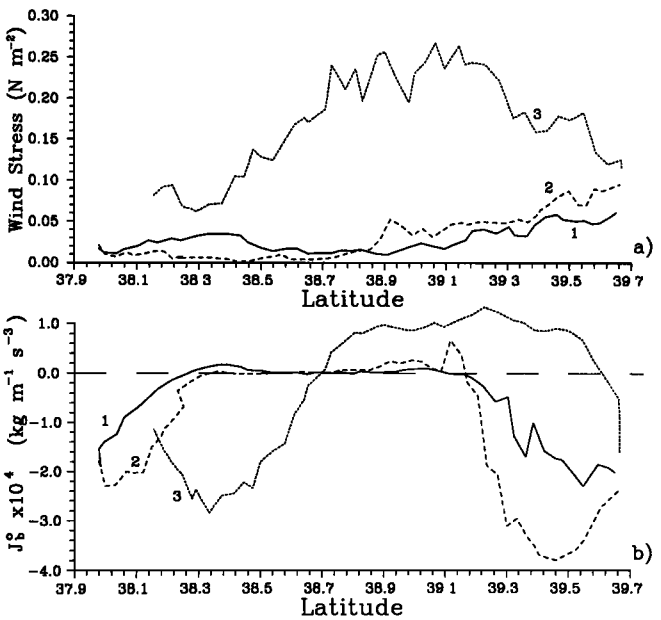

Fig. 2. (*a*) Wind stress magnitude τ_o (N m^{-2}) ($=\rho_a C_{10}\langle U_{10}^2\rangle$, where ρ_a is the density of air, C_{10} is the surface drag coefficient (~1.3×10^{-3}) [*Large and Pond*, 1981] and U_{10} is the wind speed at 10 m height) and (*b*) surface buoyancy flux J_b^o (kg m^{-1} s^{-3}) for transects 1, 2, and 3 along 125°W.

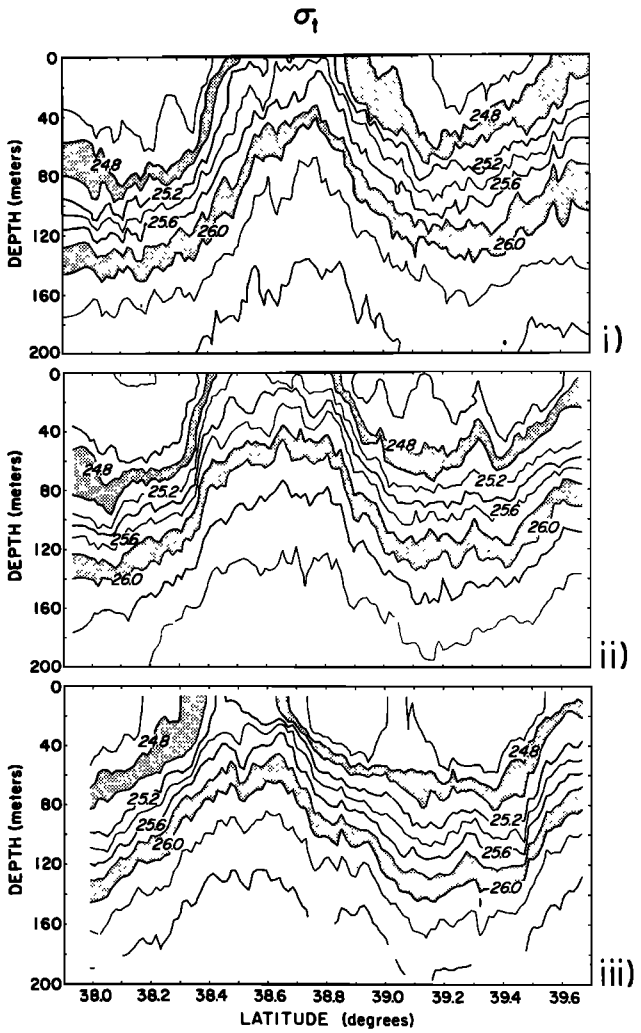

Fig. 3*a*. Contour plots of the density anomaly (σ_t) sections obtained with the RSVP microstructure system for transects 1(i), 2(ii), and 3(iii). The contour interval is 0.2 kg m^{-3}. Highlighted intervals are 26.0–25.8 and 25.0–24.8.

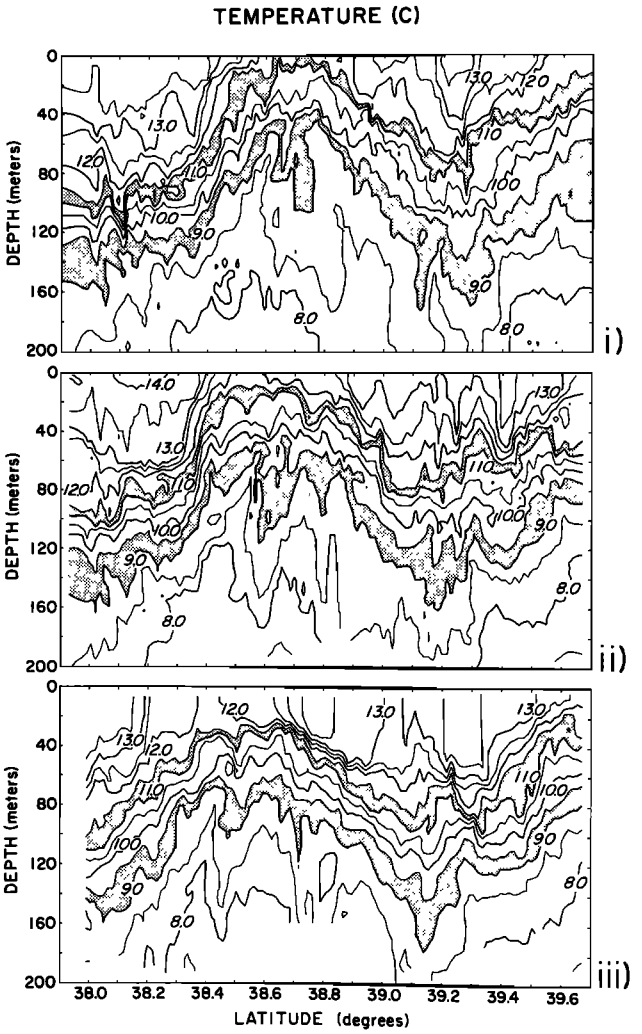

Fig. 3*b*. Contour plots of the temperature sections obtained with the RSVP microstructure system for transects 1(i), 2(ii), and 3(iii). The contour interval is 0.5°C. Highlighted intervals are 9.0°–9.5°C and 12.5°–13.0°C.

nearly vertical, an indication of horizontal density gradients within a vertically mixed surface layer. Between transects 1 and 2 the dense core translated southward slightly at all depths (Figure 4). As the winds increased from the north between transects 2 and 3, the upper layers of the dense core moved rapidly southward (20 and 60 m in Figure 4), while the change at 140 m was less rapid.

The current structure associated with the meander (Figure 3*d*) shows strong onshore (eastward) flow to the south of the core and strong offshore (westward) flow to the north. These narrow currents are centered over the sloping pycnocline (Figure 3*a*). The peak surface currents are on the warm side of the surface signature of the front, which represents the location where the sloping pycnocline makes contact with the surface. Although the sharp gradients associated with this outcropping are the most easily identifiable feature in the satellite image, the current associated with the front is on the warm side of the strong surface gradient. This agrees with the findings of *Kosro* [1985] investigating fronts near the continental shelf. Peak zonal currents were near the surface within the offshore flow (Figure 5), reaching nearly 100 cm s^{-1} during transect 3. In all cases the net transport in the upper 150 m across the entire feature (between 38°N and 39.2°N) was offshore (~1 Sv).

The dynamic height field was computed from smoothed RSVP hydrographic sections. Relative geostrophic velocities perpendicular to the sections were estimated. To reduce the effects of internal waves, the gridded hydrographic data were smoothed using a Laplacian (∇^2) filter with vertical and horizontal half-power cutoffs of 24 m and 13 km, respectively. The horizontal cutoff wavelength represents about one-half the Rossby deformation radius, the horizontal scale at which rotation effects become as important as buoyancy effects. The filter removes most of the internal wave variability while leaving the structure of the large scale unchanged.

Since RSVP profiles extended only to 200 m, geostrophic velocities could not be referenced to a level of no motion. To obtain reasonable estimates of the near-surface geostrophic velocities, relative geostrophic velocities at 150 m were set equal to the navigated (and smoothed) Doppler velocities at 150 m. Surface (20 m) geostrophic velocities (Figure 6) are therefore relative to the estimated absolute velocities at 150 m. Differences between geostrophic and measured velocities

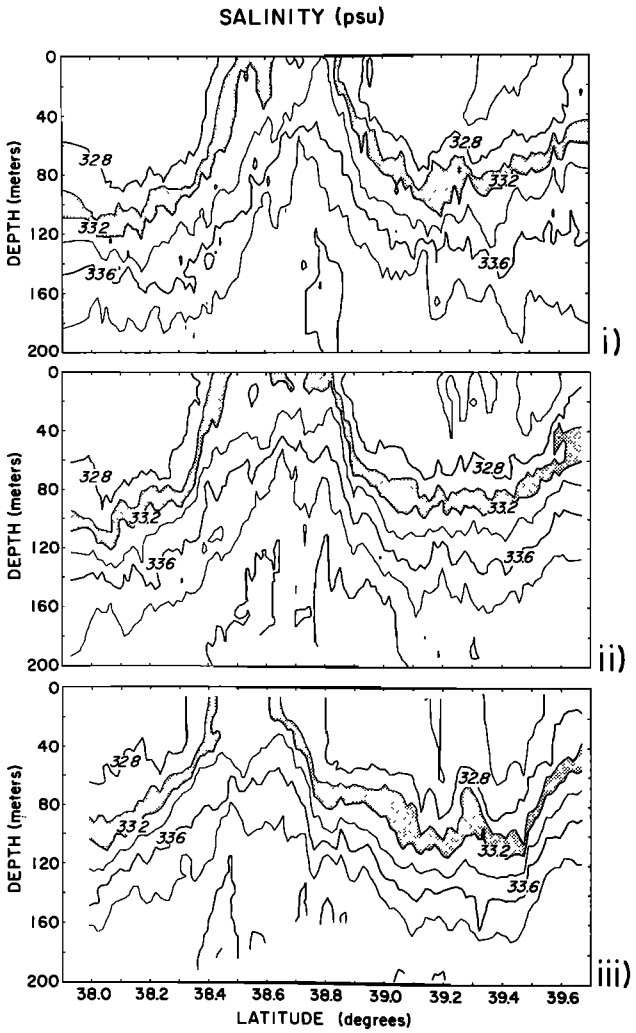

Fig. 3c. Contour plots of the salinity sections obtained with the RSVP microstructure system for transects 1(i), 2(ii), and 3(iii). The contour interval is 0.2‰. The highlighted interval is 33.0–33.2‰.

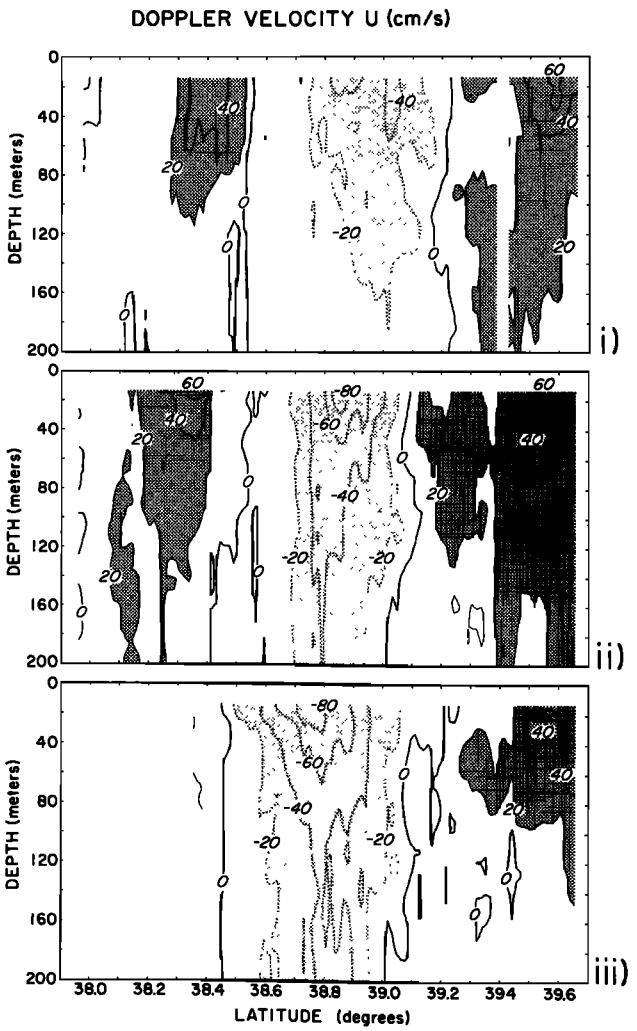

Fig. 3d Contour plots of the U (zonal) velocity sections obtained with the ship-mounted ADCP system for transects 1(i), 2(ii), and 3(iii). The contour interval is 20.0 cm s^{-1}.

at 20 m are attributable to ageostrophic structure above 150 m. Linear regressions between the geostrophic and Doppler velocity estimates at 20 m for the three transects give correlation coefficients of $r_1 \simeq 0.95$, $r_2 \simeq 0.96$, $r_3 \simeq 0.96$ and regression coefficients of $b_1 \simeq 1.04$, $b_2 \simeq 1.09$, $b_3 \simeq 1.11$. The rms difference between the geostrophic and Doppler velocity estimates at 20 m for all transects is ~10 cm s^{-1}.

Some features of the ε sections (Figure 3e) can be qualitatively related to the large-scale structure. Below the pycnocline, ε was consistently low, near the noise level of the RSVP (~10^{-9} W kg^{-1}). The raised pycnocline within the core of the meander therefore results in relatively low ε values at middepth (50 m). This agrees with the findings of *Moum et al.* [1988], who found low values of ε at middepths within a cool rotating feature west of Oregon. Regions of large ε (>10^{-7} W kg^{-1}) were confined to the surface mixing layer (Figures 3a and 3e). When winds increased to ~13 m s^{-1} during transect 3, a deepened, actively mixing layer formed across the entire region (Figure 3e, panel iii). Within the core of the feature, where the pycnocline was near the surface, wind-induced turbulence clearly caused enhanced mixing through the pycnocline.

4. Pycnocline Erosion: Mixed and Mixing Layers

To clearly identify the effects of surface-induced mixing on the pycnocline, the meander was divided into regions determined by proximity to the core of the feature. The data were averaged into five regions: region i, south of the meander; region ii, south front (strong onshore flow); region iii, core of the meander; region iv, north front (strong offshore flow); and region v, north of the meander (Figures 7a–7c). Differences in the average $\langle \sigma_t \rangle$ profiles across the feature highlight the raised pycnocline in the core region (always between 38.4° and 38.8°N). Apparent in the contour plots (Figure 3e) and the averaged profiles (Figures 7a–7c) are reduced turbulent dissipation rates below the pycnocline. Within the core region (Figure 7, region iii), low values of ε ($\leq 5.0 \times 10^{-9}$ W kg^{-1}) start at a depth of ~50 m; outside the meander, this level is not reached until ~150 m. This is likely due to two conditions existing in the core region: (1) the proximity of the pycnocline to the surface (~5–20 m (Figure 8)) inhibits surface-generated mixing from penetrating to deeper water, and (2) the currents and shears were small within the core, resulting in lower turbulence production. However, we were unable to find a strong correlation

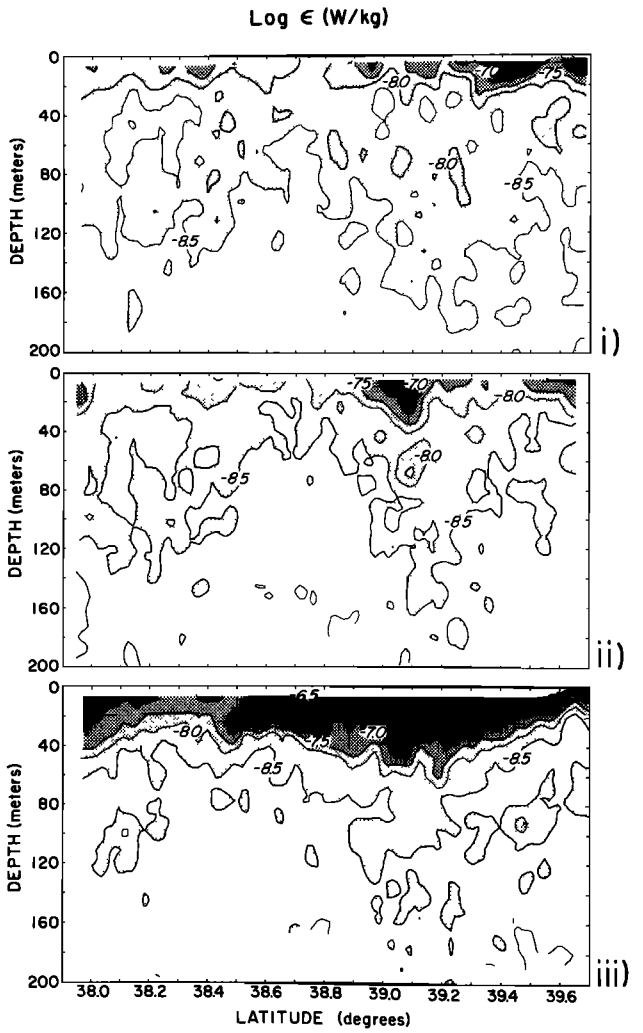

Fig. 3e. Contour plots of log of the turbulent dissipation rate [log (ε)] in units of W kg^{-1} or m^2 s^{-3} obtained with the RSVP for transects 1(i), 2(ii), and 3(iii). The contour interval is 0.5.

between ε and current shear and therefore believe that the former mechanism explains the observed distribution of ε.

The most significant variation in ε was related to temporal changes in the intensity of mixing in the near-surface region due to variations in wind stress. The wind stress was determined as $\tau_o = \rho_a C_{10} \langle U_{10}^2 \rangle$, where ρ_a is the density of air, C_{10} is the surface drag coefficient ($\sim 1.3 \times 10^{-3}$) [*Large and Pond*, 1981], and U_{10} is the wind speed at 10 m height. The response in the near-surface layers to increased wind stress was rapid. An actively mixing turbulent layer extending to the pycnocline developed within an hour after the onset of stronger winds.

When mixing extends into the pycnocline, denser water is entrained to the surface. Satellite images before and after significant wind events often reveal the strengthened temperature signals, presumably due to this entrainment of cool water from below [*Flament et al.*, 1985]. Spatial variations in pycnocline depth may result in localized areas of enhanced entrainment. In section 6 this variability is postulated as a possible mechanism for maintaining the signature of the feature.

A clear distinction must be made between mixed and mixing layers due to the fact that the mechanics of turbulence is altered in the presence of stratification. It is only in a stratified fluid that turbulence does work to alter the density structure. In a truly mixed layer, vertical turbulent motions are unaffected by buoyancy forces. When turbulence penetrates to the stratified pycnocline, turbulent motions do work against the restoring force of gravity. Some portion of the kinetic energy exerted against the force of gravity is irreversibly retained in the newly mixed density field and represents potential energy gained by the mixed layer.

Mixed layers represent an integrated history of mixing events, and may not be actively mixing (turbulent) at the time of measurement. In fact, it has been common practice to refer to the mixed layer as the upper layer of the ocean above the seasonal pycnocline, even though it may be neither truly mixed (unstratified) nor mixing. To our knowledge, the only truly unstratified mixed layer is convectively driven. The depth of the actively mixing layer can be determined from $\varepsilon(z)$ profiles. We define the depth of the mixing layer as the depth at which ε drops below 5.0×10^{-9} W kg^{-1}. The mixed layer depth can be determined from σ_t profiles and will be estimated by the depth at which σ_t has increased by 0.1 kg m^{-3} above the near-suface σ_t value. Figures 8*a*, 8*b*, and 8*c* show the value of σ_t within the mixed layer, the depth of the mixed layer, and the depth of the actively mixing layer across the entire region for transects 1, 2, and 3, respectively. Since gradients in both σ_t and ε are quite strong at the bases of mixed and mixing layers, respectively, choosing different indicators for identifying the mixed and mixing layer depths (e.g., $\Delta\rho \sim 0.05$ and $\varepsilon < 10^{-8}$) has little effect on the layer depths.

Our comparison of mixed and mixing layer depths indicates that during lighter winds ($U_{10} < 5$ m s^{-1}) the mixing layer is deeper than the mixed layer only where the pycnocline is shallow (<20 m). Otherwise the mixed layer tends to be deeper than the mixing layer. Only during the higher winds ($U_{10} \simeq 13$ m s^{-1}) of transect 3 was the mixing layer deeper than the mixed layer over the entire region. When the mixing layer depth exceeds the mixed layer depth, turbulent entrainment takes place across the pycnocline, whereas entrainment cannot occur where mixing does not penetrate the pycnocline (that is, where the mixing layer depth is less than the mixed layer depth). Mixed layer models such as those described by *Denman* [1973] and *Niiler and Kraus* [1977] provide estimates of the turbulent buoyancy flux (or turbulent entrainment across the pycnocline) parameterized in the terms of surface wind forcing, but they do not account for the effect of varying pycnocline, or mixed layer depth. Our observations suggest that such bulk parameterizations may be inadequate near oceanic fronts. To compare our direct measurements with the model parameterizations, a closer look at the components of the near-surface energy equation is required.

5. Conversion of Mixing Layer Kinetic Energy To Mixed Layer Potential Energy

Parameterizing the rate of gain of potential energy (PE) within the mixed layer as a function of wind stress (or wind speed) is an essential element of modeling the mixed layer [e.g., *Denman and Miyake*, 1973, *Niiler and Kraus*, 1977, *Davis et al.*, 1981; *Rudnick and Davis*, 1988]. Direct observations that can be used to estimate the parameterization are

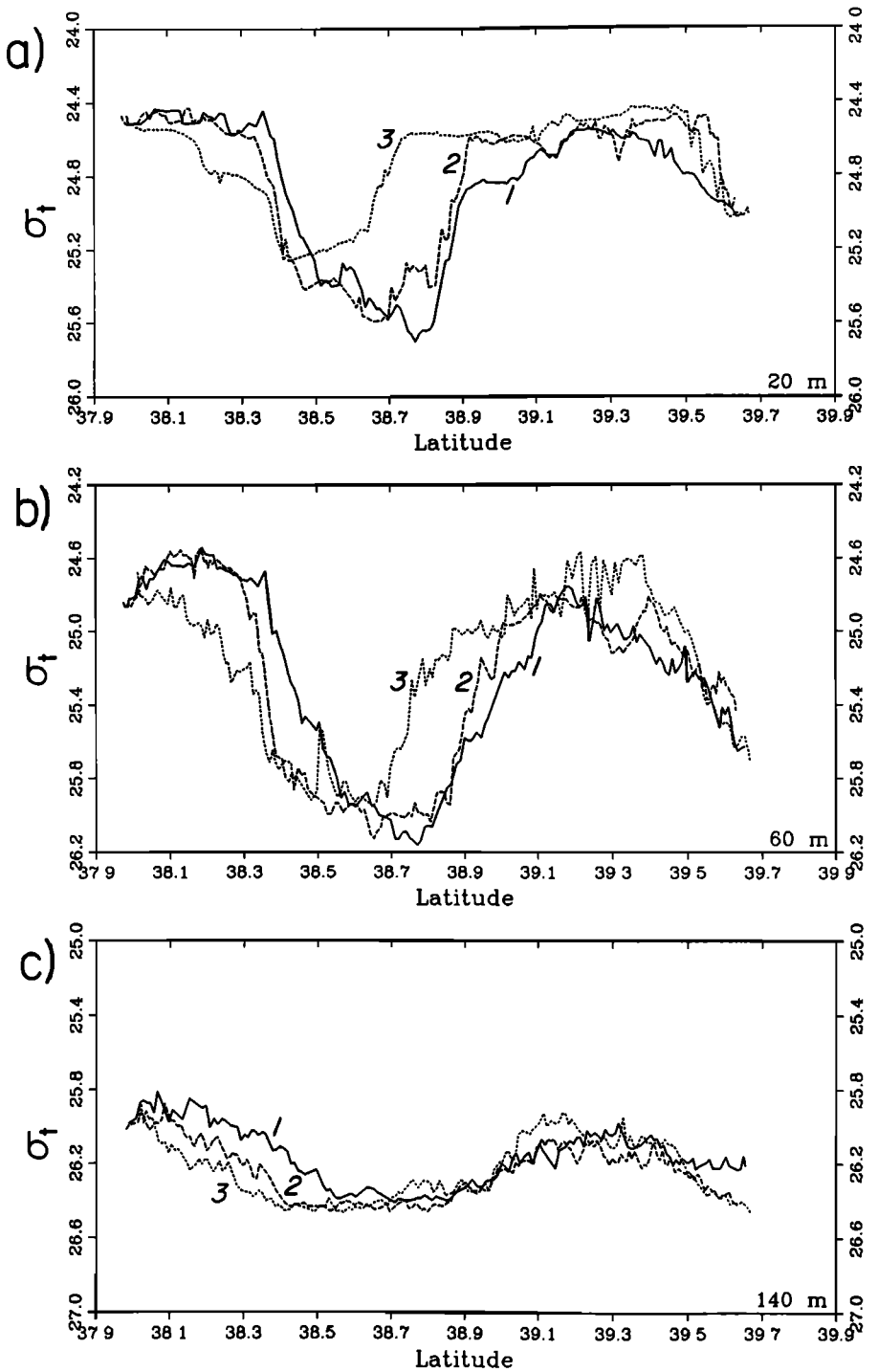

Fig. 4. Density anomaly (σ_t) at fixed depths (*a*) 20 m, (*b*) 60 m, and (*c*) 140 m for the three transects. Only slight changes are present at depth (140 m) between the transects, the south front moving steadily southward. Nearer the surface a considerable change can be seen between the first two transects, when the wind was light, and the third transect, when moderate winds blow from the north.

rare [*Denman and Miyake*, 1973; *Davis et al.*, 1981]. Estimates of the proportion of wind energy that is (1) dissipated within the surface layer and (2) converted into potential energy through turbulent buoyancy fluxes have been reported by a number of the authors mentioned above. The vertically integrated turbulent buoyancy flux J_I through the surface mixing layer is equal to the rate of change of PE of the surface mixed layer and can be parameterized by the nondimensional parameter m, where $J_I = mE_{10}$ and E_{10} is the rate of working by the wind stress at a height of 10 m given by $E_{10} = \tau_o \overline{U}_{10}$.

Denman and Miyake [1973] described observations of the wind-forced mixed layer at station P in the northeast Pacific. They found good agreement between a surface mixed layer model [*Denman*, 1973] and observations (variation in mixed layer depth over time) when 0.12% of the wind energy (at a

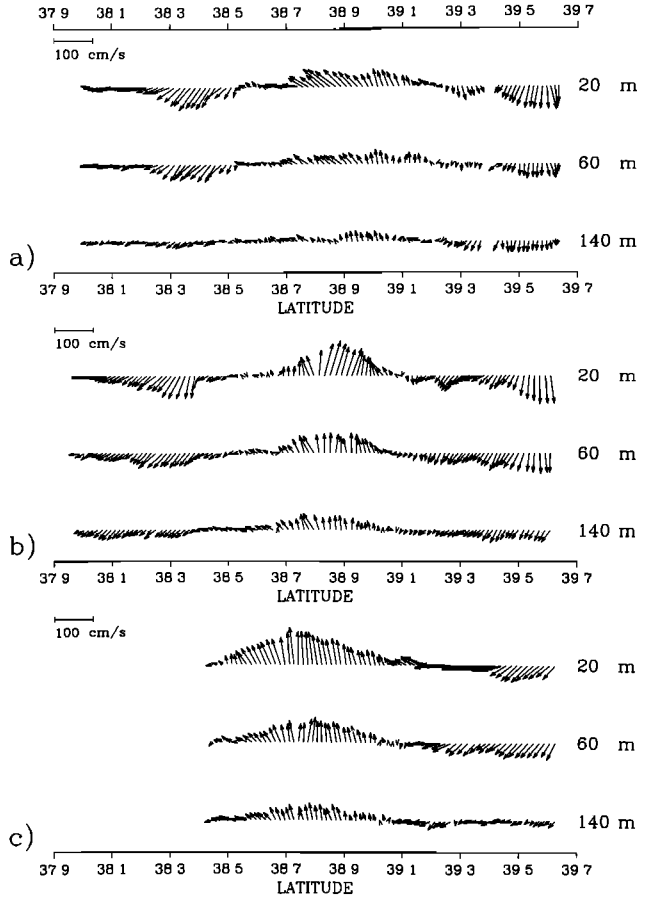

Fig. 5. Current vectors obtained with the ship-mounted ADCP at depths of 20 m, 60 m and 140 m for (*a*) transect 1, (*b*) transect 2, and (*c*) transect 3. There are no vectors shown for the southern portion of transect 3 due to poor navigation. The first Doppler bin is at a depth of 15.1 m; subsequent bins are spaced at 4-m intervals. A time average of 15 min has been applied to the raw data, resulting in a horizontal spacing of approximately 1.5 km. For the current vectors, north is to the right.

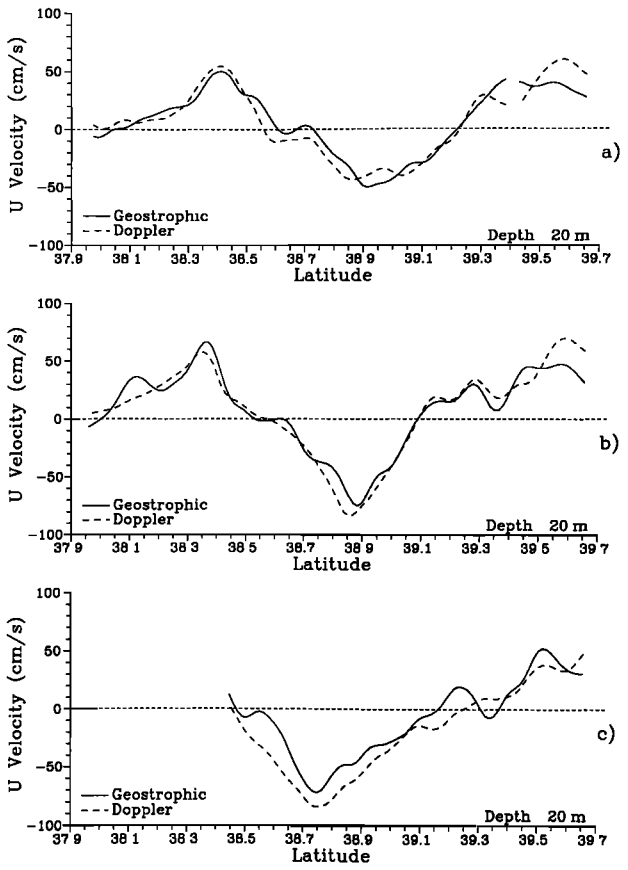

Fig. 6. Estimated zonal geostrophic velocities (solid) and measured Doppler U velocities (dashed) at 20 m for (*a*) transect 1, (*b*) transect 2, and (*c*) transect 3. The geopotential anomaly was calculated from the RSVP data, filtered at 13 km in the horizontal and 27 m in the vertical. The geostrophic velocities were set equal to the measured Doppler velocities at a depth of 150 m. North is to the right, offshore flow is negative U, and onshore positive U. On average, the correlation coefficient is $r \simeq 0.96$ with an rms difference between the Doppler and geostrophic of ~ 10 cm s^{-1}.

height of 10 m) is assumed to be converted into PE within the mixed layer, or $m \simeq 0.0012$. *Denman and Miyake* [1973] define an estimate of the turbulent energy flux through a level just below the surface due to wind forcing as $E_0 \equiv \rho_o u_*^3 \simeq (\rho_a C_{10}/\rho_o)^{1/2} E_{10}$ (where ρ_o is the density of water at the surface and u_* is the friction velocity at the surface of the ocean). Upon substitution their results predict that 100% of this turbulent energy flux below the surface is converted into PE, $J_I \simeq E_0$.

Turner [1969] used observations from *Stommel et al.* [1969] that indicate as much as 1% of E_{10}, or $\sim 8E_0$ is converted into mixed layer PE. *Richman and Garrett* [1977] estimated that between 4 and 9% of E_{10} crosses the air-sea interface, including the energy that goes into surface wave generation. Of this, they estimate 1% goes into increasing the PE of the surface mixed layer. This is equivalent to $J_I \simeq (0.4\text{–}0.9)E_0$. *Davis et al.* [1981] arrive at a similar result, $J_I \simeq 0.5E_0$, by comparing model results with measurements made during the Mixed Layer Experiment (MILE).

The bulk proportions m ($=J_I/E_{10}$) and m_0 ($=J_I/E_0$) may in fact be inherently variable on short time scales, as the actual rate of turbulent kinetic energy (TKE) input and rate of increase of PE in the surface layer of the ocean depend not only on τ_0 but on the sea state, the energy input by breaking waves, the shear from inertial motions, buoyancy flux at the surface, and the depth of the mixed layer over which E_0 is dissipated.

From a flux Richardson number argument [*Osborn*, 1980], one may expect that the average increase in PE gain is less than 20% of the integrated dissipation rate through the surface mixing layer, or $J_I \leq 0.2\varepsilon_I$. We calculate the integrated dissipation rate through the mixing layer, ε_I, following *Oakey and Elliott* [1982]. The dissipation rate in the very near surface layer is assumed equal to the shallowest ε value measured. The shallowest dissipation rate, uncontaminated by ship wake, is typically between $z \sim -5$ and -8 m. This calculation probably underestimates the true ε_I, which may have larger contributions in the very near surface layer [*Oakey and Elliott*, 1982]. The ratio of the integrated dissipation rate ε_I to the subsurface energy flux parameter E_0 will be denoted $m_\varepsilon = \varepsilon_I/E_0$. Calculating the integrated turbulent buoyancy flux J_I and therefore obtaining an estimate of m_0 requires more attention.

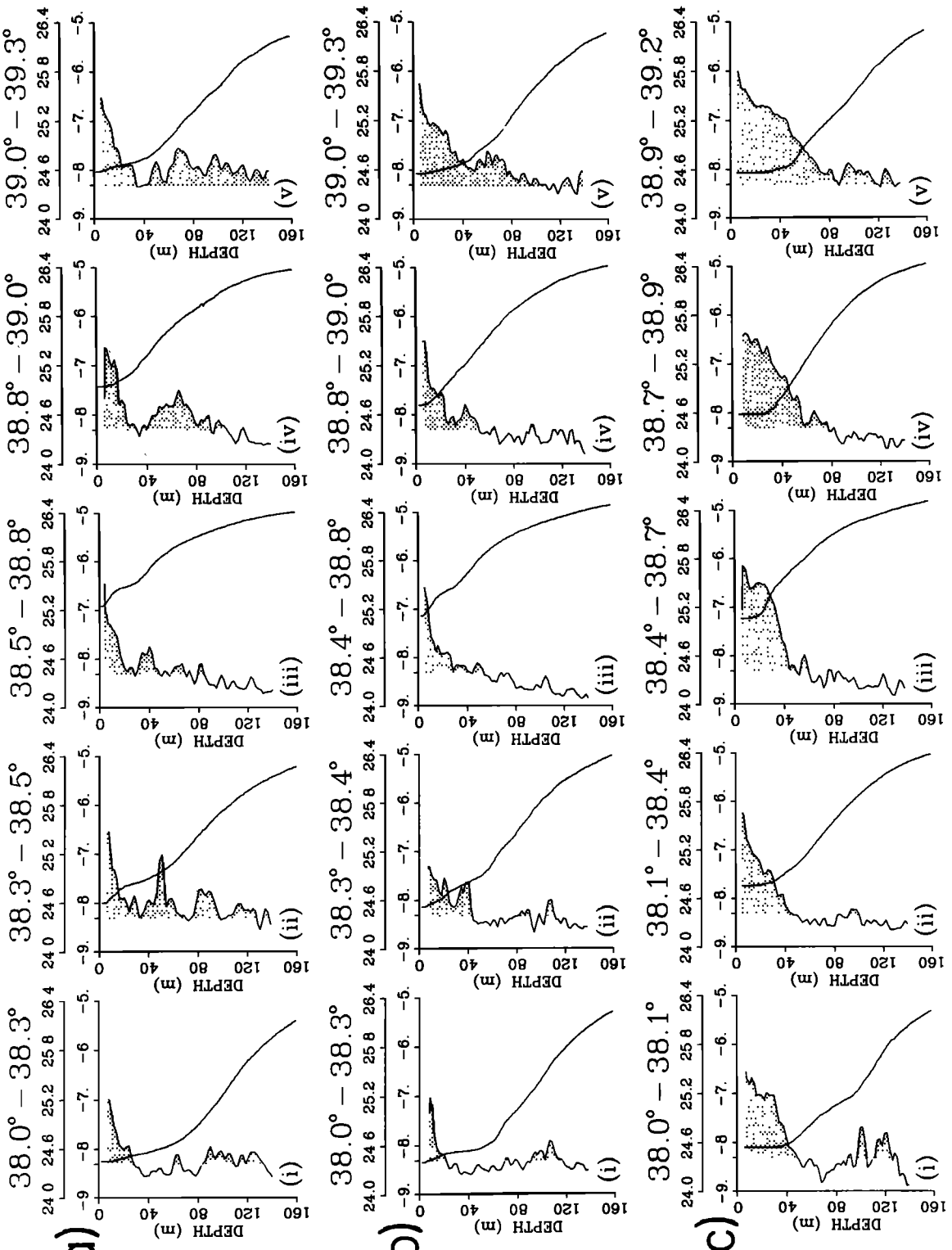

Fig. 7. Average profiles of log $\langle\bar{\varepsilon}\rangle$ and $\langle\sigma_t\rangle$ for (*a*) transect 1, (*b*) transect 2, and (*c*) transect 3. The profiles have been averaged into five meridional regions encompassing the meander. These regions were determined from the velocity data (Figure 3*d*) and are region i, south of the meander; region ii, the south front or onshore flow region; region iii, the core or central region; region iv, the north front or offshore flow region; and region v, north of the meander. Shaded areas indicate dissipation rates greater than 5.0×10^{-9} W kg^{-1}. Note that the latitude ranges for the different regions change slightly from transect to transect.

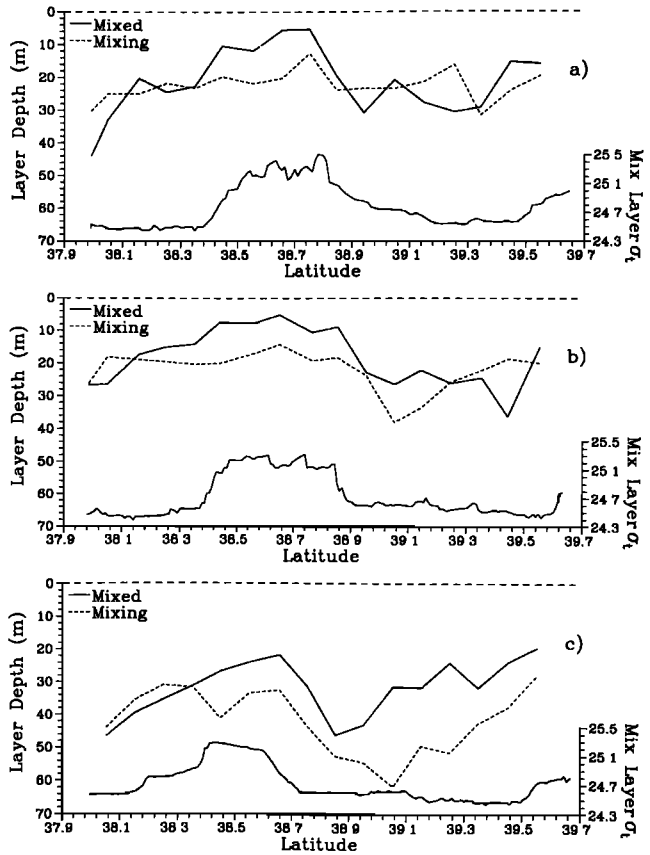

Fig. 8. Values of σ_t within the mixed layer and the depth of the mixed (solid) and mixing (dashed) layers for (*a*) transect 1, (*b*) transect 2, and (*c*) transect 3. The depth of the mixed layer is where σ_t has increased to 0.1 above the surface value. The mixing layer depth is determined from the dissipation rate profiles $\varepsilon(z)$ as the depth where ε drops below 5.0×10^{-9} W kg^{-1}. Layer depths were computed from individual RSVP profiles and averaged into 0.1° latitude bins.

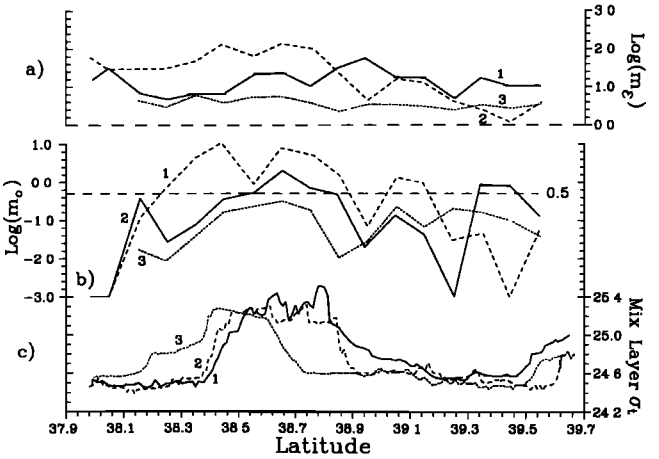

Fig. 9. Shown for each transect 1, 2, and 3 are 0.1° averaged values of the log of the ratio $m_\varepsilon (= \varepsilon_I/E_0)$, the integrated dissipation rate to the subsurface energy flux rate (Figure 9*a*), and the log of the ratio m_0 ($= J_I/E_0$), the integrated turbulent buoyancy flux (proportional to the gain in potential energy within the mixing layer) and the subsurface energy flux rate (Figure 9*b*). Zero values of m_0 occur when the mixing layer is shallower than the mixed layer; these values have been set equal to 10^{-3} for this logarithm plot. *Davis et al.* [1981] arrive at the result $m_0 = 0.5$ by comparing model results with measurements made during MILE. Also shown is the value of σ_t at the surface (Figure 9*c*).

The turbulent energy balance equation for the surface mixed layer is given in detail by *Niiler and Kraus* [1977]. For our purposes the steady state energy balance integrated across the surface mixing layer may be written as

$$\int_{-h}^{0} [P - g\langle w'\rho'\rangle - \rho\varepsilon]\, dz = 0 \qquad (1)$$

where flux divergence and advective terms have been omitted, and what remain are (1) the rate of TKE production (P), (2) the rate of conversion of TKE into PE through turbulent buoyancy flux, and (3) the rate of TKE dissipation, $\rho\varepsilon$. The distinction between mixed and mixing layers implies that the correct depth h to use in equation (1) is the depth of the mixing layer. Contributions to the turbulent buoyancy flux are nonzero only where the stratification is nonneutral ($N^2 > 0$, or $\rho' \neq 0$). Our integrated mixing layer energy equation can then be rewritten as

$$\int_{-h_\varepsilon}^{0} P\, dz = \int_{-h_\varepsilon}^{0} [\rho\varepsilon]\, dz + \int_{-h_\varepsilon}^{-h_\rho} [g\langle w'\rho'\rangle]\, dz \qquad (2)$$

This form has units of watts per square meter, $-h_\varepsilon$ is the depth of the mixing layer, and $-h_\rho$ is the depth of the mixed layer.

In our case this is an oversimplification because our "mixed" layers are weakly stratified and some buoyancy flux is necessary to transport dense fluid from the top of the pycnocline. In the analysis to follow, our interest is in determining the net rate of change of average mixed layer density. We assume an actively mixing mixed layer in which J_b acts to rapidly redistribute fluid vertically.

To estimate the turbulent buoyancy flux $J_b (= g\langle\omega'\rho'\rangle)$, the parameterization introduced by *Osborn* [1980] is adopted, for which an upper bound to the turbulent buoyancy flux is

$$J_b \leq (0.2\rho\varepsilon) \qquad (3)$$

This parameterization yields nonzero J_b in an unstratified mixed layer where no work is done against buoyancy forces; hence the importance of our distinction between h_ε and h_ρ. Having stated that $\int_{-h_\rho}^{0} [g\langle\omega'\rho'\rangle]\, dz = 0$, we integrate J_b only over the depth of penetration of mixing into the pycnocline ($-h_\varepsilon < z < -h_\rho$). The integrated dissipation rate is defined by $\varepsilon_I \equiv \int_{-h_\varepsilon}^{0} (\rho\varepsilon)\, dz$, and the integrated turbulent buoyancy flux by $J_I \equiv \int_{-h_\varepsilon}^{-h_\rho} (0.2\rho\varepsilon)\, dz$.

Shown in Figure 9 are the spatial series of the estimated quantities m_ε and m_0 (note that $m = (\rho_a C_{10}/\rho_o)^{1/2} m_0 \simeq 0.0012 m_0$) for each of the three transects. For the consistently high winds of transect 3, the ratio of integrated dissipation, m_ε, is very nearly constant ($\langle m_\varepsilon\rangle \simeq 4 \pm 1$). During these stronger winds (~13 m s^{-1}) the ratio m_ε shows little dependence on proximity to the fronts. However, the ratio m_0 shows considerable variation across the feature. Within the core region, $\langle m_0\rangle \sim 0.7$. Just north and south of the core region, where the pycnocline is deeper, the ratio drops by more than a factor of 10, $\langle m_0\rangle \sim 0.03$. At the very north end of the transect the pycnocline shallows (Figure 8),

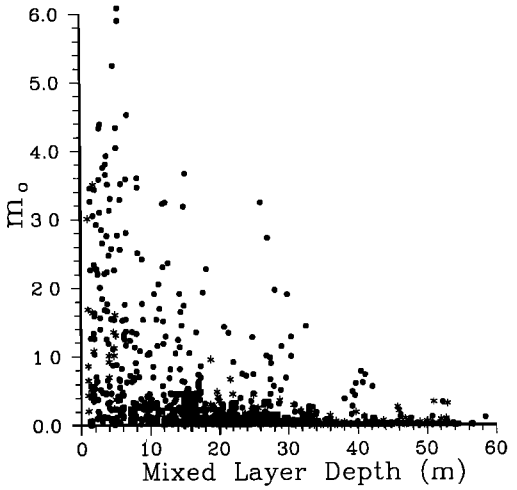

Fig. 10. Individual profile estimates of the ratio of mixed layer potential energy gain to wind-generated turbulent energy flux, m_0 (= J_I/E_0) plotted against mixed layer depth h_ρ for wind stress >0.1 N m^{-2}. In addition to estimates calculated from 1987 data (asterisks), data collected in 1988 across a single-sided front have been included (circles). The correlation coefficient is $r = -0.38$ with a bootstrap standard deviation of ±0.0137. There are a total of 804 points. The integral length scale computed from the autocorrelation is ~7 km. The ratio of total spatial series over the integral length scale suggests 82 independent observations of m_0 versus h_ρ. A value of $|r| > 0.22$ is significantly different from zero at the 95% confidence level.

and m_0 increases to 0.5. While the values estimated for m_0 within the cool filament are similar to the estimates discussed above, the value of m_0 outside the filament is smaller by as much as a factor of 10. Since our J_b estimate may be an upper bound, the estimates for m_0 should also be considered upper bounds.

In Figure 10 the m_0 values obtained from individual profiles during moderate winds ($\tau_o > 0.1$ N m^{-2}) are plotted against mixed layer depth. There is a consistent trend toward larger m_0 values where the mixed layer is shallow. The higher m_0 values are distributed evenly in space across the frontal regions. It is the variations in mixed layer depth that result in the horizontal variability of J_I and therefore m_0. Horizontal variability in m_0 is not usually taken into account in models and might more realistically be parameterized by including a dependence on pycnocline, or mixed layer depth.

The mean m_0 from all three 1987 transects (Figure 9) is $\langle m_0 \rangle \simeq 1.0 \pm 0.34$, where the uncertainty represents one standard deviation. This is exactly the value used by *Denman and Miyake* [1973]. Although it appears serendipitous, we believe our mean value is too large due to the high m_0 values estimated during very light winds and at night when E_0 underestimates the available turbulent kinetic energy when surface buoyancy flux may provide the dominant source for mixing. The mean value for m_0 from transect 3 only (when winds were strong) is ~0.12 ± 0.03, smaller than most values used in models.

Although a trend relating m_0 to mixed layer depth is apparent in the data (Figure 10), we hesitate to fit a regression to them. Observations in regions such as the northern Pacific, where fall storms induce sufficient mixing to reach the permanent thermocline below 100 m, might greatly change the appearance of Figure 10. Our data also suggest there is considerable fine-scale variability in m_0, and we expect that extensive sampling is required before a more general relation is formulated relating m_0 and mixed layer depth. Also, by neglecting buoyancy flux within the mixed layer we may be underestimating m_0 for the deeper mixed layers. It is also believed that long-term deepening of the mixed layer depends on inertial motions generated by the onset of strong winds. Such conditions would increase the net buoyancy flux, yielding a larger effective m_0.

Nelson et al. [1989] suggest that a variable entrainment rate with nitrocline depth results in enhanced primary production within a Gulf Stream warm-core ring. Their analysis of the potential energy gain within the warm-core ring, where the pycnocline is near the surface, using $m_0 = 0.5$ was found to underestimate the amount of nutrient flux required for the observed biomass plume. Had they considered a form for m_0 that depends on pycnocline depth, the local maxima in phytoplankton biomass within the warm-core ring might have been explained without the need for large episodic wind-mixing events.

From our estimates of J_I and m_0 we can determine the surface forcing required to establish an equilibrium state in which the heating of the surface mixed layer by surface buoyancy fluxes J_b^o balances cooling by turbulent buoyancy fluxes at the base of the mixed layer. For a mixed layer depth of 5 m, a linear fit to the data in Figure 10 predicts $m_0 \simeq 0.63$. A daily mean of $\langle J_b^o \rangle \simeq -1.0 \times 10^{-4}$ kg m^{-1} s^{-3} would be balanced by an equal and opposite turbulent buoyancy flux through the base of the mixed layer when the wind speed is $U_{10} \simeq 5$ m s^{-1}. The same wind acting on a deeper mixed layer would result in reduced entrainment, and the temperature of the deeper mixed layer would slowly increase, and/or restratify. This is counter to suggestions that a shallow mixed layer gains heat faster than a deep mixed layer based simply on considerations of volume.

If the right-hand side of (2) represents the sinks for the surface layer TKE, and E_0 is some measure of the TKE flux at the surface due to wind stress, then one may expect the two to be correlated. In Figure 11 the combined TKE sinks through the surface mixing layer ($\varepsilon_I + J_I$) are plotted against E_0. J_I is always much smaller than ε_I and at most contributes ~10% to the sum ($\varepsilon_I + J_I$). The data include both June 1987 and July 1988 data, where in 1988, 13 transects were made across a single-sided front. During lighter winds ($E_0 < 5.0 \times 10^{-4}$ W m^{-2}) the integrated dissipation and buoyancy flux are independent of wind forcing. At higher wind speeds ($E_0 > 5.0 \times 10^{-4}$ W m^{-2}) the data exhibit a clear trend. A linear fit to the high wind speed data yields ($\varepsilon_I + J_I$) $\simeq (3.5 \pm 1.7) E_0^{1.0 \pm 0.1}$). The break in the data was determined objectively to minimize the standard deviations in the slopes of the low- and high-wind regions. This compares to the equivalent result of *Oakey and Elliott* [1982], who obtained $\varepsilon_I \simeq 6.5 E_0$, where they integrate ε through the mixed layer only. Based on the combined uncertainty estimates, these results are in agreement. The total TKE sinks ($\varepsilon_I + J_I$) have no dependence on proximity to fronts, and the data for all regions have been included in the regression.

6. Does Differential Entrainment Affect Frontal Dynamics?

The observation of variable entrainment rate with proximity to the front leads to the generation of horizontal density gradients (frontogenesis) within the surface mixed layer. In this section we investigate the effect this may have

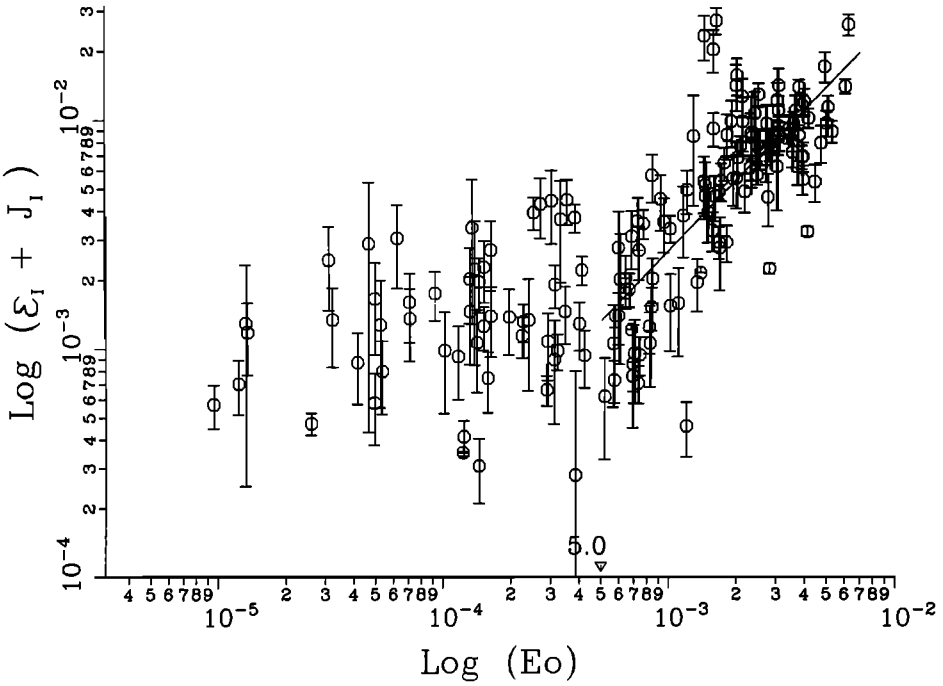

Fig. 11. Combined turbulent kinetic energy sinks within the surface mixing layer ($\varepsilon_I + J_I$) versus the subsurface energy flux rate $E_0(= \rho_o u_*^3)$. The data were objectively split into two groups, low wind ($E_0 < 5.0 \times 10^{-4}$) and high wind ($E_0 > 5.0 \times 10^{-4}$), and a linear fit ($(\varepsilon_I + J_I) = (3.5 \pm 1.7)E_0^{1.0 \pm 0.1}$)) has been applied to the high-wind data. The data include 1987 and 1988 measurements and have been averaged into 0.1° latitude bins (approximately 10 estimates per bin) with error bars indicating ±1 standard deviation.

on fronts and propose a mechanism which may lead to an acceleration of the surface mixed layer in the direction of the preexisting geostrophic flow.

Rudnick and Davis [1988] discuss three conditions that lead to frontogenesis. Similar to the studies of *deSzoeke* [1980] and *deSzoeke and Richman* [1981], who drive frontogenesis with horizontal variations in the wind stress field, *Rudnick and Davis* [1988] suggest two possible frontogenetic processes that rely on mixed layer/lower layer convergences and divergences. A third frontogenetic process described by *Rudnick and Davis* [1988] enhances an existing frontal structure through wind-forced mixing only. Within their two-layer model, the frontal structure is enhanced (pycnocline shallowing) in regions where the density interface (pycnocline) is already nearer the surface, and wind-induced mixing (some prescribed fraction of E_0) results in entrainment. The observations presented here qualitatively support the model results of *Rudnick and Davis* [1988]. A direct comparison between the model and our observations is not possible because of the simplistic parameterization of the two-layer model.

To examine the effect of a spatially variable rate of converting wind-induced turbulent kinetic energy (E_0) into surface layer buoyancy flux (J_b) on a frontal structure, we consider variations in the rate of change of surface mixed layer density due to mixing across the pycnocline. The rate of change of density within the mixed layer due only to vertical mixing across the pycnocline (not including advection or convection) can be written as

$$\frac{\partial \rho}{\partial t} = -\frac{1}{g}\frac{\partial J_b}{\partial z} \tag{4}$$

Horizontal variations in J_b within the surface mixing layer imply variations in the rate of change of density within the surface mixed layer. To see the effect these horizontal density anomalies have on the mean flow, we consider the time rate of change of the zonal thermal wind equation,

$$\frac{\partial}{\partial t}\left[\frac{\partial U}{\partial z} = \frac{g}{f\rho}\frac{\partial \rho}{\partial y}\right] \tag{5}$$

Integrating (5) through the surface mixing layer, from the surface to the depth of near-zero turbulent dissipation, gives

$$\frac{\partial}{\partial t}\int_{-h_\varepsilon}^{0}\frac{\partial U}{\partial z}\,dz \simeq \frac{g}{f\rho_o}\frac{\partial}{\partial y}\int_{-h_\varepsilon}^{0}\frac{\partial \rho}{\partial t}\,dz \tag{6}$$

where $-h_\varepsilon$ represents a maximum mixing layer depth. Upon substitution of (4) into (6) and splitting the integrals into two layers, the surface mixed layer and the layer between the mixed and mixing layer depths where turbulent buoyancy fluxes contribute, we have

$$\frac{\partial}{\partial t}\left[\int_{-h_\rho}^{0}\frac{\partial U}{\partial z}\,dz + \int_{-h_\varepsilon}^{-h_\rho}\frac{\partial U}{\partial z}\,dz\right] \simeq \frac{1}{f\rho_o}\left[\int_{-h_\rho}^{0}\frac{\partial (J_b)}{\partial z}\,dz + \int_{-h_\varepsilon}^{-h_\rho}\frac{\partial (J_b)}{\partial z}\,dz\right] \tag{7}$$

where $-h_\rho$ is the depth of the mixed layer and must be shallower than the maximum mixing layer depth $-h_\varepsilon$. The first integrals on either side of (7), through the near neutrally stratified mixed layer, are assumed to be negligible. This

follows by assuming that a mixed layer cannot support shear ($\int_{-h_\rho}^{0} (\partial U/\partial z)\, dz = 0$) and that there is no turbulent buoyancy flux within the interior of a mixed layer ($\int_{-h_\rho}^{0} (\partial (J_b)/\partial z)\, dz = 0$). Upon integrating the remaining terms in (6) we obtain

$$\left.\frac{\partial U}{\partial t}\right|_{-h_\rho} - \left.\frac{\partial U}{\partial t}\right|_{-h_\varepsilon} \simeq \frac{1}{f\rho_0}\frac{\partial}{\partial y}\left[(J_b)|_{-h_\rho} - (J_b)|_{-h_\varepsilon}\right] \quad (8)$$

At the base of the mixing layer the turbulence is weak, and the turbulent buoyancy flux is negligible. Considering only accelerations relative to the base of the mixing layer, we may write the acceleration of the mixed layer relative to the base of the mixing layer due to horizontal variations in pycnocline erosion as

$$\frac{\partial U}{\partial t} \simeq \frac{1}{f\rho_0}\frac{\partial}{\partial y}\left[J_b(-h_\rho)\right] \quad (9)$$

where $J_b(-h_\rho)$ represents the turbulent buoyancy flux at the base of the mixed layer. Equation (9) implies that horizontal variations in the turbulent buoyancy flux in the pycnocline result in an acceleration of the mixed layer. The sign of (9) is such that when this process acts on an oceanic front, the result is always to accelerate the surface layer in the direction of the geostrophic flow, thereby acting to maintain the signature of the front.

To evaluate the effect of the proposed mechanism for maintaining frontal dynamics, we estimated J_b using (3), so that

$$\frac{\partial U}{\partial t} \simeq \frac{0.2}{f\rho_0}\frac{\partial}{\partial y}\left[\rho\varepsilon(-h_\rho)\right] \quad (10)$$

where $\varepsilon(-h_\rho)$ can be determined from our microstructure data. The acceleration predicted by (10) is likely to be an overestimate. Vertical mixing which results in enhanced horizontal density gradients ($\partial\rho/\partial y$) represents stored potential energy. The relaxation of the available potential energy (APE) into kinetic energy is not as efficient as (5) would imply. The adjustment toward geostrophy may only convert a portion (about one-third) of the APE into kinetic energy [*Gill*, 1982].

During transect 3, conditions existed (moderate (> 13 m s^{-1}) winds and a mixing layer penetrating to the pycnocline) such that the left-hand side of (10) predicts nonzero mixed layer acceleration ($\partial U/\partial t$). The horizontal gradients of the dissipation rate at the base of the mixed layer ($\Delta(\rho\varepsilon(-h_\rho))/\Delta y$) were of the order of $\sim(5.0 \times 10^{-3}/10)$ W m^{-3} km^{-1}. From (10) these gradients predict that the mixed layer could be accelerated by $O(1)$ cm s^{-1} d^{-1} in the direction of the preexisting geostrophic flow. This acceleration is small but suggests that when winds of moderate strength have sufficient duration, the mixed layer near the fronts may be enhanced and accelerated by differential entrainment across the front. During clear summer weather off northern California it is not uncommon to have sustained winds for periods of several days, in which case the cumulative effect of the noted surface acceleration could be considerable (in excess of 10% of the mean flow). During periods when winds in the CTZ study region are much larger (~40 knots or ~20 m s^{-1}), the rate of entrainment over a shallow pycnocline could be 10 times the rate observed here. The surface layer density gradient established under these conditions might result in measurable acceleration.

While differential erosion of the pycnocline by surface layer mixing increases the horizontal density gradient at the surface, the same process reduces the horizontal density gradient below the mixed layer. Deceleration of the geostrophic flow may then be expected below the surface mixed layer where the isopycnal slopes are reduced. The net result is that this mechanism increases the vertical shear, or baroclinicity, of the frontal system.

Unfortunately, it is impossible to test our hypothesis from the data. Many competing effects act to accelerate the fronts, and it is impossible to determine the relative contributions from each. Perhaps a more comprehensive three-dimensional survey would be necessary to reveal the effect.

Satellite observations of similar frontal structures reveal considerable variability [*Flament et al.*, 1985] and indicate possible surface relaxation/enhancement under calm/windy conditions. This may be due to the following sequence of events. Under calm conditions the very near surface water is homogeneously (on a synoptic scale) heated or cooled by the surface buoyancy flux, smoothing the surface signature of the fronts. During moderate to high winds, surface mixing erodes through any locally heated surface stratification, entraining cooler water from below. Subsequent satellite images reaffirm the location of the rejuvenated cool anomalies, revealing the subsurface structure. Entrainment will be more efficient near the fronts and where the pycnocline is nearer the surface. The steepened isopycnals in the mixed layer resulting from this vertical entrainment represent stored PE, which may result in enhanced surface currents upon relaxation.

7. Conclusions

Measurements of oceanic microstructure and surface meteorology across fronts indicate that wind-generated turbulence is more effective in entraining dense, cool water to the surface on the cool side of the front where the pycnocline is nearer the surface. Estimates of the ratio of energy input by the wind and potential energy gained by entrainment can vary by more than a factor of 10 across the observed fronts. Mixed layer models might more accurately parameterize the energy balances by including the effect of variable pycnocline depth on m_0.

The detection of these features by AVHRR satellite imagery relies on strong surface temperature gradients. By defining mixed layer depth from the density structure and mixing layer depth from turbulent dissipation rate measurements, we have estimated larger turbulent buoyancy fluxes where the pycnocline is closer to the surface. Hence we expect that under appropriate conditions (moderate winds) the rate of increase of mixed layer density (and potential energy) is greater on the cool (dense) side of fronts, thereby maintaining the signature of the front.

Detailed examination of cool filaments in the coastal transition zone reveal two important features:

1. Isopycnals rising toward the dense core, in approximate agreement with geostrophy, raise the pycnocline by 50 m or more.

2. The raised pycnocline within the filament acts as a shallow barrier to surface-forced mixing, resulting in anomalously low values of ε at depths intermediate between the

pycnocline within the filament and the pycnocline outside the filament.

A simple model was posed to evaluate the effect on the frontal dynamics of differential entrainment across the front. The model suggests a possible means for accelerating the surface currents of a preexisting frontal structure while maintaining the cool surface signature. No observations of the feature were made following the strong winds, and direct observations of the ensuing current enhancement are not available. Because of the highly variable and changing nature of these filamentlike structures on time scales of a few days, it is unlikely that the estimated surface accelerations ($\sim$1 cm s^{-1} d^{-1}) would be detectable at any rate. Under extreme wind conditions (wind speeds of 30–40 knots) (15–20 m s^{-1}), the entrainment/acceleration process described may result in current enhancement of several centimeters per second per day. It is likely that the process described here is only one of the many mechanisms responsible for causing variability in the features. Certainly, other processes act to erode the front (e.g., mesoscale eddy formation) at different rates. We have simply attempted to quantify the effect of a single, simple mechanism in maintaining a preexisting frontal structure.

Acknowledgments. The authors would like to thank Doug Caldwell, Clayton Paulson, and Roland deSzoeke for comments on an early draft; Dave Hebert for fruitful discussions; and Clayton Paulson for providing surface meteorological data. This work was sponsored by the Office of Naval Research under contract N00014-87-K-0242.

REFERENCES

Bernstein, R. L., L. Breaker, and R. Whritner, California current eddy formation: Ship, air and satellite results, *Science*, *195*, 353–359, 1977.

Brink, K. H., The near-surface dynamics of coastal upwelling, *Prog. Oceanogr*, *12*, 223–257, 1983.

Caldwell, D. R., T. M. Dillon, and J. N. Moum, The rapid-sampling vertical profiler: An evaluation, *J. Atmos. Oceanic Tech.*, *2*, 615–625, 1985.

Chereskin, T. K., J. N. Moum, P. J. Stabeno, D. R. Caldwell, C. A. Paulson, L. A. Regier, and D. Halpern, Fine-scale variability at 140°W in the equatorial Pacific, *J. Geophys. Res.*, *91*, 12,887–12,897, 1986.

Davis, R. E., R. deSzoeke, and P. P. Niiler, Variability in the upper ocean during MILE, 2, Modeling the mixed layer response, *Deep Sea Res.*, *28A*, 1453–1475, 1981.

Denman, K. L., A time-dependent model of the upper ocean, *J. Phys. Oceanogr.*, *3*, 173–184, 1973.

Denman, K. L., and M. Miyake, Upper layer modification at ocean station Papa: Observations and simulation, *J. Phys. Oceanogr.*, *3*, 185–196, 1973.

deSzoeke, R. A., On the effects of horizontal variability of wind stress on the dynamics of the ocean mixed layer, *J. Phys. Oceanogr.*, *10*, 1439–1454, 1980.

deSzoeke, R. A., and J. G. Richman, The role of wind-generated mixing in coastal upwelling, *J. Phys. Oceanogr.*, *11*, 1534–1547, 1981.

Flament, P., L. Armi, and L. Washburn, The evolving structure of an upwelling filament, *J. Geophys. Res.*, *90*, 11,765–11,778, 1985.

Gill, A. E., *Atmosphere-Ocean Dynamics*, *Int. Geophys. Ser.*, vol. 30, 662 pp., Academic, San Diego, Calif., 1982.

Huyer, A., Coastal upwelling in the California current system, *Prog. Oceanogr.*, *12*, 259–283, 1983.

Ikeda, M., and W. J. Emery, Satellite observations and modeling of meanders in the California current system off Oregon and northern California, *J. Phys. Oceanogr.*, *14*, 1434–1450, 1984.

Kosro, P. M., Shipboard acoustic current profiling during the Coastal Ocean Dynamics Experiment, *SIO Ref. 85-8*, Scripps Inst. of Oceanogr., La Jolla, Calif., 1985.

Large, W. G., and S. Pond, Open ocean momentum flux measurements in moderate to strong winds, *J. Phys. Oceanogr.*, *11*, 324–336, 1981.

Mooers, C. M. K., and A. R. Robinson, Turbulent jets and eddies in the California current and inferred cross-shore transports, *Science*, *223*, 51–53, 1984.

Moum, J. N., D. R. Caldwell, and P. J. Stabeno, Mixing and intrusions in a rotation cold-core feature off Cape Blanco, Oregon, *J. Phys. Oceanogr.*, *18*, 823–833, 1988.

Nelson, D. M., J. J. McCarthy, T. M. Joyce, and H. W. Ducklow, Enhanced near-surface nutrient availability and new production resulting from the frictional decay of a Gulf Stream warm-core ring, *Deep Sea Res.*, *36*(5), 705–714, 1989.

Niiler, P. P., and E. B. Kraus, One-dimensional models of the upper ocean, in *Modelling and Predictions of the Upper Layers of the Ocean*, edited by E. B. Kraus, pp. 153–172, Pergamon, New York, 1977.

Oakey, N. S., and J. A. Elliott, Dissipation within the surface mixed layer, *J. Phys. Oceanogr.*, *12*, 171–185, 1982.

Osborn, T. R., Estimates of the local rate of vertical diffusion from dissipation measurements, *J. Phys. Oceanogr.*, *10*, 83–89, 1980.

Richman, J., and C. Garrett, The transfer of energy and momentum by wind to the surface mixed layer, *J. Phys. Oceanogr.*, *7*, 876–881, 1977.

Rudnick, D. L., and R. E. Davis, Frontogenesis in mixed layers, *J. Phys. Oceanogr.*, *18*, 434–457, 1988.

Stommel, H., K. Saunders, W. Simmons, and J. Cooper, Observations of the diurnal thermocline, *Deep Sea Res.*, *16*, suppl., 269–284, 1969.

Turner, J. S., A note on wind mixing at the seasonal thermocline, *Deep Sea Res.*, *16*, suppl., 297–300, 1969.

R. K. Dewey and J. N. Moum, College of Oceanography, Oregon State University, Oceanography Admin. Bldg. 104, Corvallis OR 97331.

(Received September 25, 1989;
accepted December 13, 1989.)